Strength properties of nanoporous materials: Molecular Dynamics computations and theoretical analysis

S. BRACH[a], K. ANOUKOU[b], D. KONDO[b], G. VAIRO[c]

a. California Institute of Technology, Division EAS, Pasadena, USA. brach@caltech.edu

b. Université Pierre et Marie Curie, Institut Jean le Rond D'Alembert, Paris, France.

c. Università degli Studi di Roma "Tor Vergata", DICII, Rome, Italy.

Résumé :

On étudie d'abord les propriétés de résistance des matériaux nanoporeux à l'aide de simulations de Dynamique Moléculaire. Ces simulations numériques sont conduites sur une cellule de monocristal d'aluminium contenant un nanopore sphérique, sous des conditions de chargements multiaxiaux en vitesse de déformation. Afin de rendre compte des traits spécifiques issus des résultats de ces simulations, une approche par analyse limite cinématique a été développée en considérant une sphère creuse avec une matrice ductile sensible aux trois invariants isotropes des contraintes. Le critère macroscopique qui en résulte dépend de manière significative des trois invariants du tenseur des contraintes macroscopique ainsi que de la taille du nanopore.

Abstract :

In this paper, the strength properties of nanoporous materials are investigated by means of Molecular Dynamics computations and theoretical analyses. Numerical calculations are carried out by considering an aluminium single-crystal embedding a spherical nanovoid, and undergoing triaxial strain conditions. A homogenization approach based on a kinematic limit analysis is derived, by considering a hollow-sphere model with a rigid-ideal-plastic solid matrix and undergoing axisymmetric strain-rate boundary conditions. As a result, the influence of pressure sensitivity and stress-Lode-angle effects on material strength properties is clearly quantified, and void-size effects are thoroughly documented.

Mots clefs : Nanoporous materials, Molecular Dynamics, Limit Analysis

1 Introduction

Interest in conceiving engineering devices based on nanoporous materials compared to conventional porous ones (i.e., with relatively larger characteristic void size) arose from the discovery that, by opportunely calibrating pore dimension at the nanoscale, it is possible to deliberately prescribe specific size-related effects at the macroscale. Accordingly, and with particular reference to mechanical features, one of the actual core research focus consists in identifying and describing the strength properties of nanoporous materials for a fixed porosity level and as dependent on the size of voids. As a matter of fact, experiments (e.g., [8]) conducted on nanoporous foams with constant porosity revealed a significant increase in the measured yield strength when void size reduces (see Fig. 1a), opening towards the development of challenging ultra-high performance devices with tailorable properties.

Molecular Dynamics simulations can be considered as effective methods to provide benchmarking evidence on nanoporous materials, allowing also to separately control a number of possible coupled effects. Specifically, although atomistic mechanisms underlying void growth and coalescence have been extensively addressed, a limited number of studies [9, 11, 12] has been devoted to the definition of engineering-oriented strength measures for nanoporous materials (see Fig. 1b). Moreover, current Molecular Dynamics computations are limited to the analysis of particular strength states only, obtained under uniaxial, volumetric or shear conditions, and therefore defining only few discrete points on the a-priori unknown three-dimensional strength domain. As regards theoretical modelling, although size-related effects have been extensively investigated in the elastic regime, limited attention has been paid so far to the dependence of effective strength properties on the void size [5, 6], classical plasticity theories for porous materials being generally conceived to predict porosity effects only (e.g., [7]).

Motivated by the above observations, the present paper aims to: investigating strength properties of an in-silico nanoporous sample via Molecular Dynamics computations (Section 2) by considering different loading paths with a wide range of triaxiality scenarios; establishing an engineering-oriented macroscopic strength criterion for nanoporous materials (Section 4), by including some physical indications arising from Molecular Dynamics computations, in the framework a kinematic limit-analysis approach. The following notation is adopted throughout the paper: boldface letters denote vectors and second-order tensors; symbols $\cdot$, :, and $\otimes$ refer to dot, double-dot, and tensor product operators, respectively; ∇ is the nabla operator.
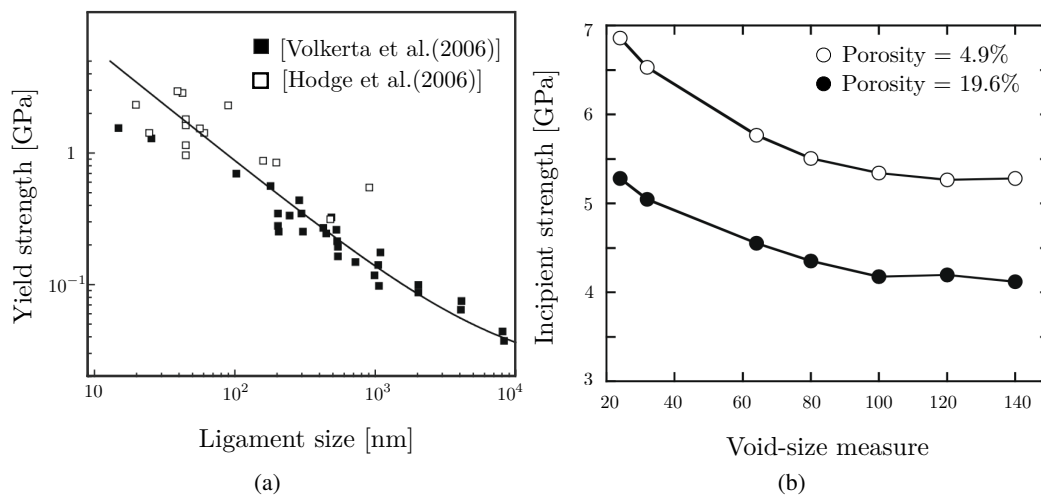

Figure 1: Void-size effects on strength properties of nanoporous materials. (a) Experimental tests. (b) Molecular Dynamics evidence [12].

2   Molecular Dynamics computations

Molecular Dynamics simulations are carried out in LAMMPS, by considering a cubic simulation box comprising a single-crystal of aluminium and a centred spherical void (see Fig. 2). The porosity f is defined as $f = 4\pi R^3/3L^3$, where R and L respectively denote the void radius and the box length. The latter is chosen such that $L/B = 10(1 + n)$, where n is an integer number and $B = a_0/2$ is the lengthscale of the Burgers vector $\mathbf{b} = B \langle 110 \rangle$ (with $a_0 = 4.04$ Å the aluminium lattice constant at room temperature). Periodic boundary conditions are applied, so that the cubic simulation domain can
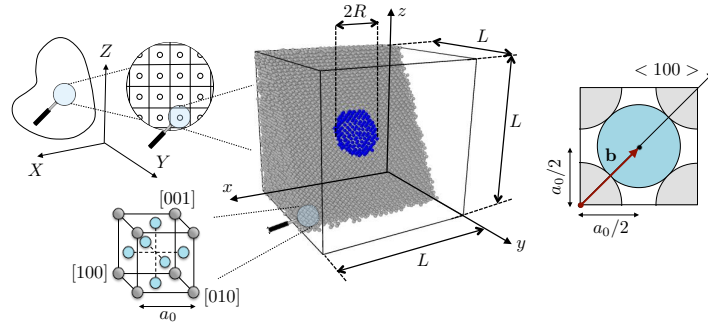
Figure 2: Computational domain. Notation.

Table 1: Values of dimensionless parameters λ, η and μ introduced in Eq. (2).

	$D_{\mathrm{m}} = 0$								$D_{\mathrm{eq}} = 0$
λ (TXE$_{\mathrm{D}}$)	-0.5	-0.4	-0.3	-0.2	-0.1	0	0.25	0.5	1
η (TXC$_{\mathrm{D}}$)	-2	-1.8	-1.6	-1.4	-1.2	-1	-0.5	0	1
μ (SHR$_{\mathrm{D}}$)	-1	$-0.8\overline{6}$	$-0.7\overline{3}$	-0.6	$-0.4\overline{6}$	$-0.\overline{3}$	0	$0.\overline{3}$	1

be considered as the representative cell of a periodic nanoporous microstructure embedding equally-spaced spherical voids. Strain-driven boundary conditions are considered, by prescribing the overall strain tensor

$$\mathbf{D}(\bar{t}) = \chi\bar{t}\left(D_{\mathrm{x}}\mathbf{e}_{\mathrm{x}} \otimes \mathbf{e}_{\mathrm{x}} + D_{\mathrm{y}}\mathbf{e}_{\mathrm{y}} \otimes \mathbf{e}_{\mathrm{y}} + D_{\mathrm{z}}\mathbf{e}_{\mathrm{z}} \otimes \mathbf{e}_{\mathrm{z}}\right) \tag{1}$$

referred to the Cartesian frame $\{\mathbf{e}_{\mathrm{x}}, \mathbf{e}_{\mathrm{y}}, \mathbf{e}_{\mathrm{z}}\}$, where $\bar{t}$ is the actual value of the time variable t, $\chi = 5 \cdot 10^9$ s^{-1} is the strain-rate parameter [9, 11, 12], and D_{x}, D_{y} and D_{z} are assigned dimensionless quantities. Strain invariants are introduced as: $I_1^{\mathrm{D}} = \mathrm{tr}\,\mathbf{D}$, $J_2^{\mathrm{D}} = \mathbf{D}_{\mathrm{d}} : \mathbf{D}_{\mathrm{d}}/2$ and $J_3^{\mathrm{D}} = \det \mathbf{D}_{\mathrm{d}}$, where $\mathbf{D}_{\mathrm{d}} = \mathbf{D} - (I_1^{\mathrm{D}}/3)\mathbf{1}$ is the deviatoric strain tensor and $\mathbf{1}$ is the second-order unit tensor. Moreover, let the following strain measures be considered: $D_{\mathrm{m}} = I_1^D/3$, $D_{\mathrm{eq}} = \sqrt{J_2^D}$ and $\cos 3\theta_{\mathrm{D}} = 3\sqrt{3}J_3^{\mathrm{D}}/[2(J_2^{\mathrm{D}})^{3/2}]$, with $\theta_{\mathrm{D}} \in [0, \pi/3]$ denoting the strain Lode angle. Aiming to investigate the mechanical response of the sample under the broadest range of triaxial conditions, three deformation paths are simulated, by adopting the following choices for quantities D_{x}, D_{y} and D_{z} in Eq. (1)

$$
\begin{aligned}
\text{TXE}_{\mathrm{D}} \quad (\theta_{\mathrm{D}} = 0) \quad &: \quad D_{\mathrm{x}} = D_{\mathrm{y}} = \lambda, \quad D_{\mathrm{z}} = 1 \\
\text{TXC}_{\mathrm{D}} \quad (\theta_{\mathrm{D}} = \pi/3) \quad &: \quad D_{\mathrm{y}} = D_{\mathrm{z}} = 1, \quad D_{\mathrm{x}} = \eta \\
\text{SHR}_{\mathrm{D}} \quad (\theta_{\mathrm{D}} = \pi/6) \quad &: \quad D_{\mathrm{x}} = 1, \quad D_{\mathrm{y}} = (1+\mu)/2, \quad D_{\mathrm{z}} = \mu
\end{aligned}
\tag{2}
$$

where dimensionless coefficients λ, η and μ are defined as summarized in Table 1, thereby allowing to range from a pure deviatoric strain condition ($D_{\mathrm{m}} = 0$) to a pure hydrostatic one ($D_{\mathrm{eq}} = 0$). The actual average stress tensor $\boldsymbol{\Sigma}(\bar{t})$ is computed via the virial formula and in agreement with the Embedded Atom Method. Corresponding stress measures $\Sigma_{\mathrm{m}} = I_1^{\Sigma}/3$ and $\Sigma_{\mathrm{eq}} = \sqrt{J_2^{\Sigma}}$, and Haigh-Westergaard invariants

$$\zeta = \frac{I_1^{\Sigma}}{\sqrt{3}}, \qquad r = \sqrt{2J_2^{\Sigma}}, \qquad \cos 3\theta_{\Sigma} = \frac{3\sqrt{3}J_3^{\Sigma}}{2J_2^{\Sigma 3/2}} \tag{3}$$

are introduced, with $I_1^\Sigma = \mathrm{tr}\,\boldsymbol{\Sigma}$, $J_2^\Sigma = \boldsymbol{\Sigma}_\mathrm{d} : \boldsymbol{\Sigma}_\mathrm{d}/2$ and $J_3^\Sigma = \det \boldsymbol{\Sigma}_\mathrm{d}$, and where $\boldsymbol{\Sigma}_\mathrm{d} = \boldsymbol{\Sigma} - (I_1^\Sigma/3)\mathbf{1}$. Triaxial stress expansion (i.e., $\theta_\Sigma = 0$), triaxial stress compression (i.e., $\theta_\Sigma = \pi/3$) and shear (i.e., $\theta_\Sigma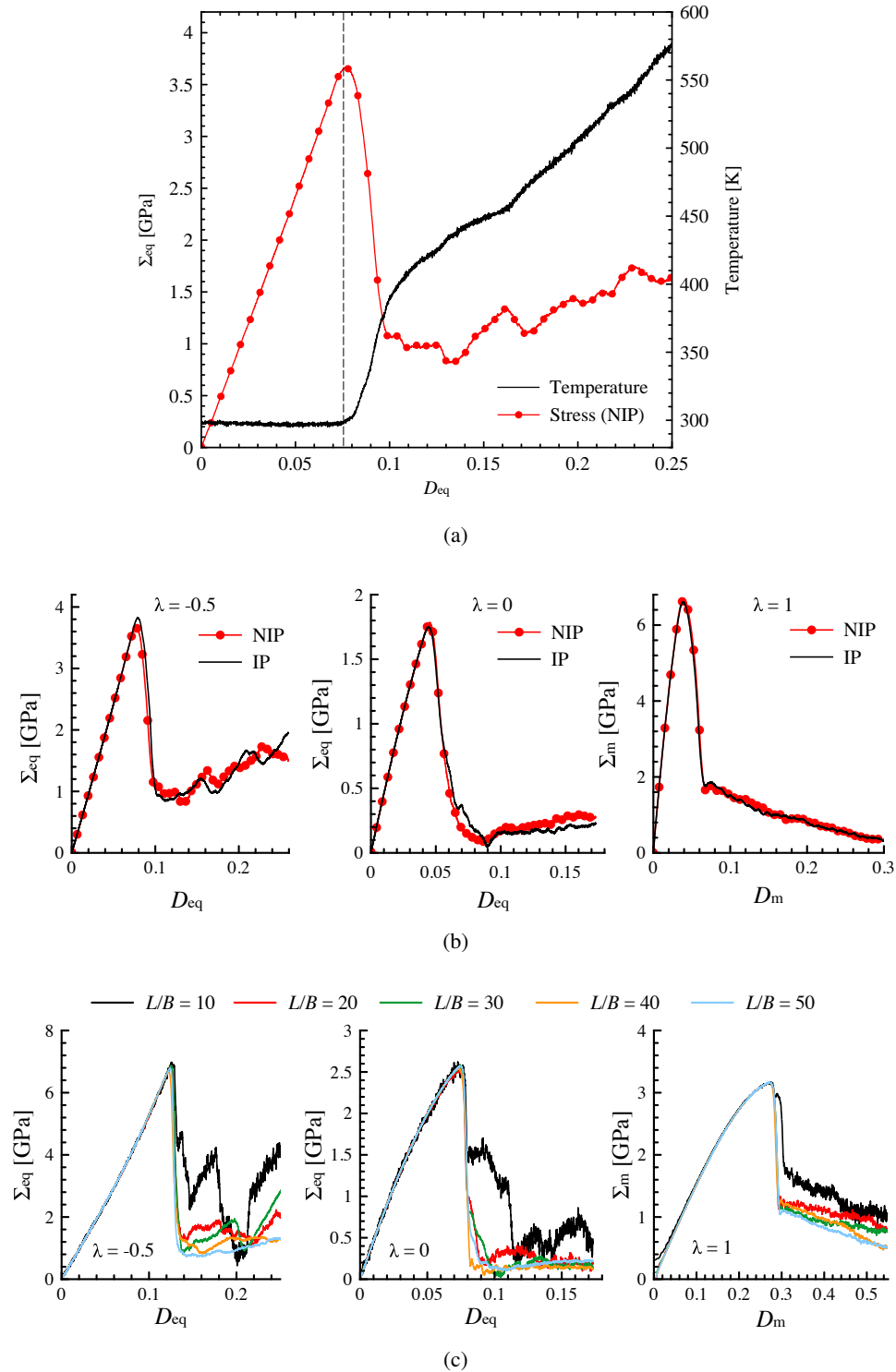 = \pi/6$) stress states are respectively denoted as TXE_Σ, TXC_Σ and SHR_Σ.

Figure 3: Deformation path TXE_D. (a) and (b) Nanoporous sample with $L/B = 50$ and $f = 1\,\%$. IP: isothermal process (at $300\,\mathrm{K}$). NIP: non-isothermal process. (c) Bulk sample ($f = 0$).

2.1 Sensitivity analyses

Aiming to furnish some indications on both temperature and periodic images effects related to the elasto-plastic deformation of the atomistic sample, some sensitivity studies have been preliminarily conducted. Main results are analyzed by referring to computed stress-strain relationships, whose typical evolution is depicted in Fig. 3 in the case of a TXE$_D$ deformation path. Stress peaks followed by a stress-relaxation phase can be clearly identified, thereby allowing for the identification of a critical condition for the sample. Stress-strain responses obtained by considering all the other deformation paths and triaxiality levels (see Eqs.(2) and Table 1), for both bulk (i.e., $f = 0$) and nanoporous samples, can be proven to exhibit the same characteristics and they are herein omitted for the sake of compactness.

As regards temperature effects, two different cases are simulated: an isothermal process (denoted as IP), and a non-isothermal one (NIP, no temperature control is used during the loading). Resulting stress-strain relationships are shown in Figs. 3a and 3b, with reference to a nanoporous sample ($f = 1\%$ and $R = 1.353$ nm). Figure 3a shows that, in the case of a NIP loading process, a significant increase of the overall temperature is observed after the occurrence of the stress peak. Nevertheless, comparison between IP and NIP results in Fig. 3b proves that such a considerable heating does not affect either the value of the stress peak or the strain level at which it occurs. Heating-induced effect appear to become more relevant at higher strain levels, depending on the considered traixiality scenario λ.

Long-range nature of dislocation fields combined with considered periodic boundary conditions results in the interaction of dislocations through the cell boundaries, leading to possibly non-negligible periodic image effects. The latter are expected to be more significant when the length L of the computational domain is small. With reference to a bulk atomistic sample, results in Fig. 3c depict stress-strain responses for different values of the ratio L/B. It is observed that small values of L/B induce significant discrepancies in the material mechanical response within the full plastic regime, resulting in marked sequences of stress rises and falls. On the contrary, both the value of the stress peak and the strain level at which it occurs are proven to not be affected by long-range dislocation interactions.
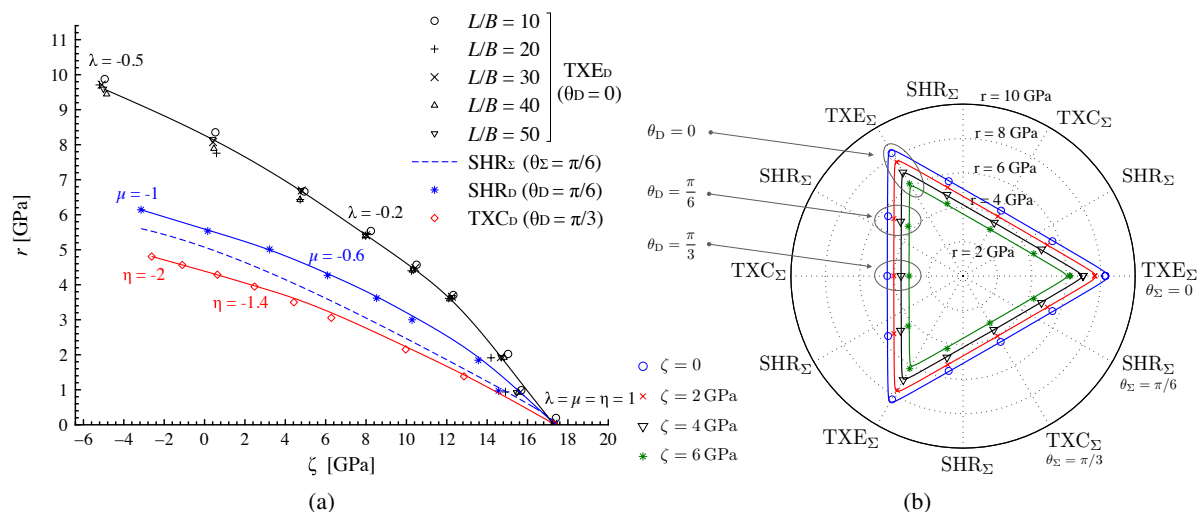

Figure 4: Bulk sample ($f = 0$). (a) Meridian strength profiles. (b) Deviatoric strength profiles. Symbols indicate computed strength states, curves represent the estimated strength profiles.
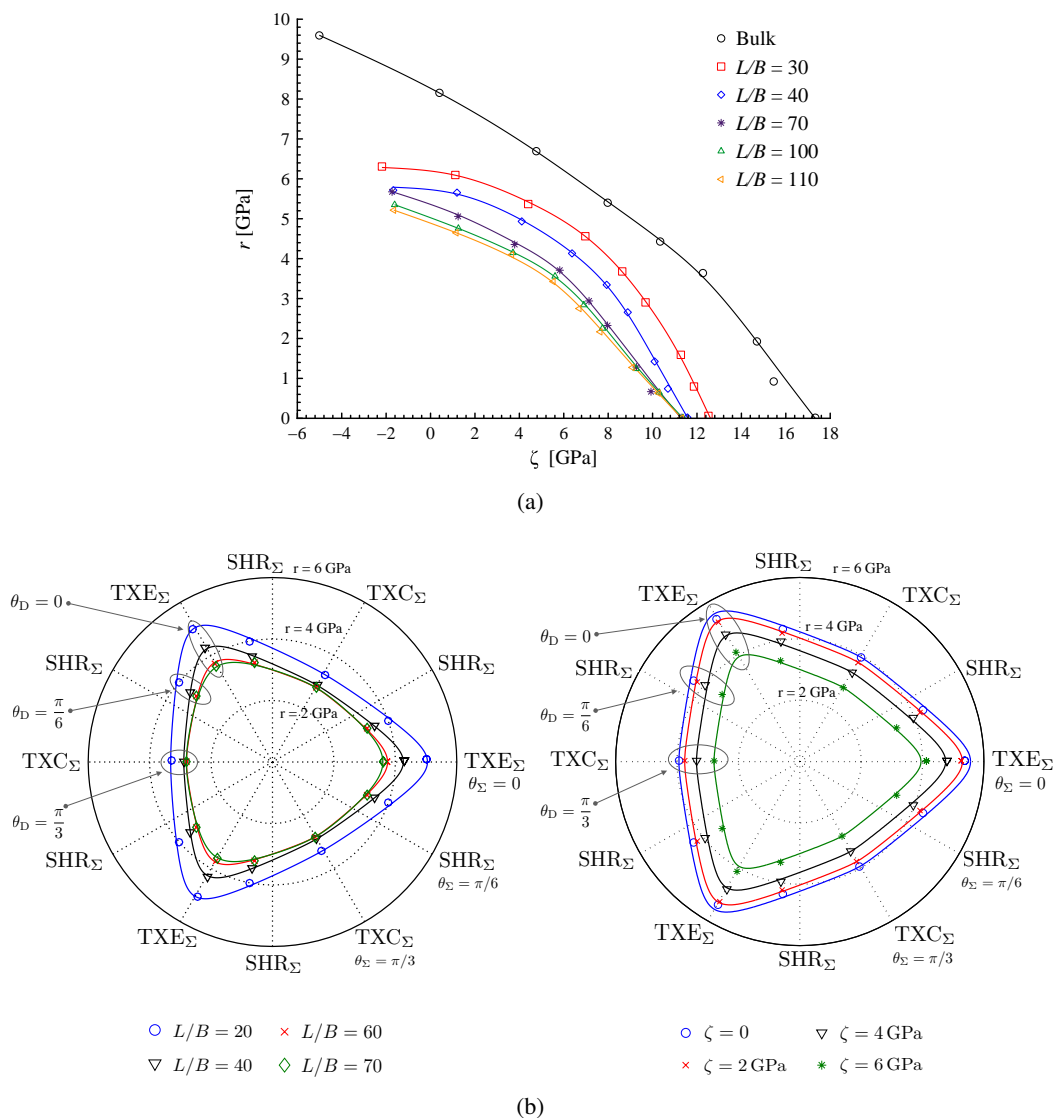
(a)

(b)

Figure 5: Nanovoided sample ($f = 1\%$). (a) Meridian strength profiles for TXE$_D$. (b) Deviatoric strength profiles: left and right figures respectively refer to cases $\zeta = 6$ GPa and $L/B = 50$. Symbols indicate computed strength states, curves represent the estimated strength profiles.

2.2 Molecular Dynamics-based strength domains

Stress peaks are assumed to identify the limit stress of the sample [9, 11, 12]. Therefore, the corresponding Haigh-Westergaard invariants in Eq. (3) allow to provide a three-dimensional representation of the material strength domain in meridian (i.e., in the plane (ζ, r) with $\theta_\Sigma = $ const) and deviatoric (i.e., in the π-plane (r, θ_Σ) with $\zeta = $ const) planes. Following results are computed with reference to an IP deformation process.

By referring to a bulk sample (i.e., $f = 0$), strength states in the space of Haigh-Westergaard coordinates $(\zeta, r, \theta_\Sigma)$ are computed in agreement with observations provided in Section 2.1, and by averaging values obtained for different ratios L/B. Corresponding meridian and deviatoric strength profiles are depicted in Figs. 4a and 4b, respectively. Strength properties of the bulk nanoscaled sample are proven to be significantly influenced by all the three isotropic stress invariants, resulting in pressure-dependent meridian (Fig. 4a) and triangular-shaped deviatoric (Fig. 4b) strength profiles. Furthermore, a strong

decoupling between the effects related to the hydrostatic stress invariant and the stress Lode angle is observed, the cross section of the material strength domain in the π-plane being the same irrespective of the considered hydrostatic component. Results in Fig. 4b also show that axisymmetric strain conditions TXE$_D$ (i.e., $\theta_D = 0$) and TXC$_D$ (i.e., $\theta_D = \pi/3$) generate stress states which are in turn practically axisymmetric $\theta_\Sigma \approx \theta_D$. On the contrary, a significant discrepancy between the strain θ_D and the stress θ_Σ Lode angles is observed in the case of shear deformation paths SHR$_D$ (i.e., $\theta_D = \pi/6$).

Figure 5 summarizes main results relevant to meridian and deviatoric strength profiles of a nanoporous sample, computed for a fixed porosity level ($f = 1\%$) and for different values of the ratio L/B (which corresponds to proportionally vary the void radius R). As in the case of the bulk sample, estimated strength properties significantly depend on all the three isotropic stress invariants, also exhibiting a strong decoupling between the influence of the hydrostatic stress and the stress Lode angle (right Fig. 5b). Moreover, triaxial strain expansion TXE$_D$ (respectively, compression TXC$_D$) practically corresponds to triaxial stress expansion TXE$_\Sigma$ (respectively, compression TXC$_\Sigma$), resulting in a good correspondence between the two Lode angles $\theta_D \approx \theta_\Sigma$. On the contrary, a major discrepancy is observed in the case of shear strain states SHR$_D$ (left Fig. 5b) Computed meridian and deviatoric strength profiles are proven to be significantly affected by void-size effects, mainly resulting in an improvement of the strength properties as the void radius R (or, equivalently, the ratio L/B) reduces. Both the occurrence and the amount of void-size effects are shown to depend on the Lode angle, the highest influence being observed in the case of triaxial-expansion stress states (left Fig. 5b). Void-size effects are also proven to induce a certain shape transition of deviatoric strength profiles, these latter passing from a multi-sided polygonal shape to a triangular-like one when the void radius reduces (left Fig. 5b).

3   From numerical evidence to theoretical modelling

Molecular Dynamics computations carried out on bulk nanoscale samples reveal on one hand a significant dependence of strength properties on all the three isotropic stress invariants, and on the other hand that such an influence can not be effectively described by yield functions classically considered in engineering approaches (e.g., Mohr-Coulomb). As such, a richer description of the local plastic behavior of nanoporous materials needs to be addressed, by including some physical indications arising from numerical simulations. To this end, a simplified form of the general yield function proposed by Bigoni and Piccolroaz [2] is considered in the following, allowing for an extreme flexibility in describing the stress-Lode-angle influence on the local plastic behavior. In detail, by referring to the cylindrical system of Lode coordinates $p = I_1^\sigma/3$, $q = \sqrt{3J_2^\sigma}$ and $\cos 3\theta_\sigma = 3\sqrt{3}J_3^\sigma/(2J_2^{\sigma\,3/2})$, with $I_1^\sigma = \text{tr}\,\boldsymbol{\sigma}$, $J_2^\sigma = \text{tr}\,\boldsymbol{\sigma}_d^2/2$ and $J_3^\sigma = \text{tr}\,\boldsymbol{\sigma}_d^3/3$ (where $\boldsymbol{\sigma}_d = \boldsymbol{\sigma} - p\mathbf{1}$ is the deviatoric part of the second-order local stress tensor $\boldsymbol{\sigma}$), the yield function $\mathcal{G}^s$ is chosen of the form

$$\mathcal{G}^s(\boldsymbol{\sigma}) = -3\left(h - \frac{p}{\xi}\right) + q\left(c_\beta \cos\theta_\sigma + s_\beta \sin\theta_\sigma\right), \tag{4}$$

with $\xi > 0$, $0 \leq \beta \leq 2$, $c_\beta = \cos(\beta\pi/6)$ and $s_\beta = \sin(\beta\pi/6)$, and where $h \geq 0$ is a strength coefficient having the dimension of a stress. In agreement with Molecular Dynamics results (see Fig. 4), Eq. (4) describes the decoupled influence of the hydrostatic invariant p and of the stress Lode angle θ_σ on local strength properties. The resulting polyhedral yield surface presents linear and multi-sided profiles in meridian and in deviatoric planes, respectively. The corresponding support function π^s is computed by applying the normality law, as detailed in [4]. Yield function in Eq. (4) also permits to properly recover
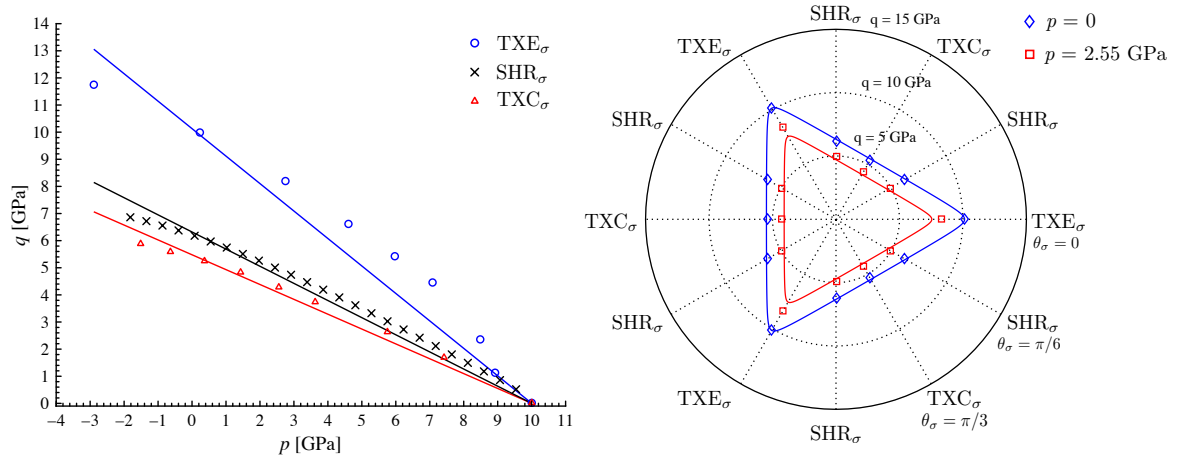
Figure 6: Calibration of the yield function $\mathcal{G}(\boldsymbol{\sigma})$ into Molecular Dynamics strength states computed in Section 2.2. Meridian (left) and deviatoric (right) strength profiles for $h = 1.82\,\text{GPa}$, $\xi = 5.48$, $\gamma = 0.99$ and $\beta = 2$. Symbols indicate Molecular Dynamics results, curves represent yield limit states $\mathcal{G}(\boldsymbol{\sigma}) = 0$.
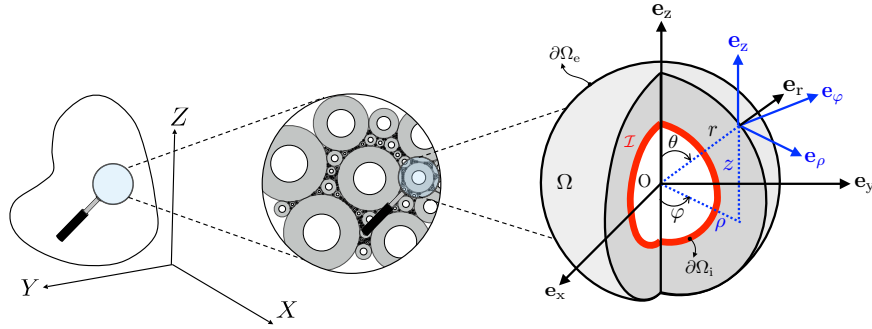

Figure 7: Representative hollow sphere. Notation.

Molecular Dynamics strength states obtained in Section 2.2 for a bulk sample, by simply calibrating model parameters ξ, β and h into numerical benchmarking evidence reported in Fig. 4. As a result, a good description of the influence of the three isotropic stress invariants on local strength properties can be provided, as shown in Fig. 6.

4 Kinematic Limit Analysis with interface effects

4.1 Problem statement

Let the hollow sphere in Fig. 7 be considered as a representative cell of a nanoporous material containing randomly-distributed spherical nanovoids. By denoting as $|\Omega_\text{v}|$ and $|\Omega_\text{s}|$ the volume measures of the solid region (that is, Ω_s) and of the void (Ω_v), respectively, the porosity f is defined as $f = |\Omega_\text{v}|/|\Omega|$ with $|\Omega| = |\Omega_\text{s}| + |\Omega_\text{v}|$. Moreover, let $\partial\Omega_\text{i}$ and $\partial\Omega_\text{e}$ indicate the internal (radius R_i) and external (radius R_e) surfaces of the hollow sphere. Referring to notation in Fig.7, let the Cartesian reference systems $(\mathbf{e}_\text{x}, \mathbf{e}_\text{y}, \mathbf{e}_\text{z})$ and $(\mathbf{e}_\text{z}, \mathbf{e}_\varphi, \mathbf{e}_\rho)$ be introduced, with the origin O at the sphere center, as well as the position vector $\mathbf{r} = r(\rho, z)\mathbf{e}_\text{r}(\varphi)$ with $r = \sqrt{\rho^2 + z^2} \in [R_\text{i}, R_\text{e}]$ and $\mathbf{e}_\text{r}(\varphi) = \mathbf{e}_\rho(\varphi) + \mathbf{e}_\text{z}$.

The excess of surface energy at the cavity boundary, due to the nanosize of the void and resulting in the occurrence of void-size effects typical of nanoporous materials, is accounted for by describing $\partial\Omega_\text{i}$ as an imperfect-coherent interface $\mathcal{I}$, through which the velocity field (resp., the stress vector) is prescribed to be continuous (resp., discontinuous). The material comprising the solid matrix Ω_s and the interface $\mathcal{I}$

is isotropic and rigid-ideal-plastic. The yield function $\mathcal{G}^{\mathrm{s}}(\boldsymbol{\sigma})$ in Eq. (4) is assumed to describe strength properties of the solid matrix. Analogously, the interface yield function $\mathcal{G}^{\mathcal{I}}(\boldsymbol{\tau})$ (with $\boldsymbol{\tau}$ the surface stress tensor at $\mathcal{I}$) is chosen of the same form as in Eq. (4). Corresponding solid matrix π^{s} and interface $\pi^{\mathcal{I}}$ support functions, as well as plastic admissibility requirements, are provided in [4].

Axisymmetric strain-rate boundary conditions are enforced at the exterior boundary $\partial\Omega_{\mathrm{e}}$ of the hollow sphere, by prescribing the homogeneous second-order strain-rate tensor

$$\mathbf{D} = D_\rho(\mathbf{e}_\rho \otimes \mathbf{e}_\rho + \mathbf{e}_\varphi \otimes \mathbf{e}_\varphi) + D_{\mathrm{z}}\mathbf{e}_{\mathrm{z}} \otimes \mathbf{e}_{\mathrm{z}} \tag{5}$$

where parameters D_ρ and D_{z} are such that $\mathbf{D}$ is non-deviatoric (i.e., $\operatorname{tr}\mathbf{D} \neq 0$). The corresponding set of kinematically-admissible velocity fields $\mathbf{v}$ is thereby defined as $\mathcal{BC}_{\mathrm{v}} = \{\mathbf{v}(\mathbf{r}) \text{ s.t. } \mathbf{v} = \mathbf{D} \cdot \mathbf{r} \quad \text{on } \partial\Omega_{\mathrm{e}}\}$. By applying the Hill's lemma, the following estimate $\widehat{\boldsymbol{\Sigma}}^{\mathrm{c}}$ of the macroscopic strength $\boldsymbol{\Sigma}^{\mathrm{c}}$

$$\widehat{\boldsymbol{\Sigma}}^{\mathrm{c}} = \frac{\partial\widehat{\Pi}(\mathbf{D})}{\partial\mathbf{D}} \tag{6}$$

is obtained, where the upper-bound estimate $\widehat{\Pi}(\mathbf{D})$ of the macroscopic support function reads as

$$\widehat{\Pi}(\mathbf{D}) = \frac{1}{|\Omega|}\left[\int_{\Omega_{\mathrm{s}}} \pi^{\mathrm{s}}(\widehat{\mathbf{d}})\, d\Omega + \int_{\partial\Omega_{\mathrm{i}}} \pi^{\mathcal{I}}(\widehat{\mathbf{d}}^{\mathcal{I}})\, dA\right] \tag{7}$$

with $\widehat{\mathbf{d}} = \operatorname{sym}\nabla\widehat{\mathbf{v}}$ and $\widehat{\mathbf{d}}^{\mathcal{I}} = \widehat{\mathbf{d}}|_{r=R_{\mathrm{i}}}$, where $\widehat{\mathbf{v}}$ is a particular trial velocity field such that $\widehat{\mathbf{v}} \in \mathcal{BC}_{\mathrm{v}}$.

4.2 Macroscopic strength criterion and illustrations

Trial velocity fields generally considered to estimate the macroscopic support function in Eq. (7) are uniquely determined by prescribing condition $\widehat{\mathbf{v}} \in \mathcal{BC}_{\mathrm{v}}$ (see for instance [7]). On the contrary, a class $\mathcal{V} = \operatorname{span}\{\widehat{\mathbf{v}}_0, \widehat{\mathbf{v}}_1\}$ of kinematically-admissible velocity fields is herein adopted, such that

$$\widehat{\mathbf{v}}_0 = \left[\left(\frac{R_{\mathrm{e}}}{r}\right)^{3\alpha} - 1\right](\rho\mathbf{e}_\rho + z\mathbf{e}_{\mathrm{z}}), \quad \widehat{\mathbf{v}}_1 = \left(D_{\mathrm{m}} - \frac{D_{\mathrm{eq}}}{2\delta}\right)\rho\mathbf{e}_\rho + \left(D_{\mathrm{m}} + \frac{D_{\mathrm{eq}}}{\delta}\right)z\mathbf{e}_{\mathrm{z}} \tag{8}$$

with $D_{\mathrm{eq}} = 2\sqrt{J_2^{\mathrm{D}}/3}$ and $\delta = 3\sqrt{3}J_3^{\mathrm{D}}/[2(J_2^{\mathrm{D}})^{3/2}]$. Kinematically-admissible velocity fields in Eq. (8) are expressed in terms of a free parameter, which allows for a certain optimization in the determination of the macroscopic strength criterion. Accordingly, by denoting as $\widetilde{\boldsymbol{\Sigma}}^{\mathrm{c}}$ the sought macroscopic strength estimate, the following inequality-constrained minimization problem is introduced

$$\mathcal{P}^* : \begin{cases} \displaystyle\min_{\widehat{\mathbf{v}}\in\mathcal{V}}\left[\widehat{\Pi} - (3\widetilde{\Sigma}_{\mathrm{m}}^{\mathrm{c}}D_{\mathrm{m}} + \widetilde{\Sigma}_{\mathrm{eq}}^{\mathrm{c}}D_{\mathrm{eq}})\right] & \text{in} \quad \Omega_{\mathrm{s}} \cup \partial\Omega_{\mathrm{i}} \\[2ex] \langle d_{\mathrm{m}}\rangle \geq \mathcal{H} & \text{in} \quad \Omega_{\mathrm{s}} \cup \partial\Omega_{\mathrm{i}} \end{cases} \tag{9}$$

where $d_{\mathrm{m}} = \operatorname{tr}\mathbf{d}/3$, $\widetilde{\Sigma}_{\mathrm{m}}^{\mathrm{c}} = \operatorname{tr}\widetilde{\boldsymbol{\Sigma}}^{\mathrm{c}}/3$ and $\widetilde{\Sigma}_{\mathrm{eq}} = \sqrt{3\widetilde{J}_2^{\Sigma}}$, and where function $\mathcal{H}$ accounts for plastic admissibility conditions on support functions π^{s} and $\pi^{\mathcal{I}}$ in an average sense. Problem $\mathcal{P}^*$ is solved via Karush-Kuhn-Tucker (KKT) conditions, thereby resulting in the following expression of the Lagrange-KKT multiplier λ

$$\lambda = 3h\xi\,\frac{f^{1-\alpha} - f - 3f\kappa\epsilon\Psi_{\mathrm{m}}^{\mathcal{I}}}{f^{1-\alpha} - f + \epsilon\Psi_{\mathrm{m}}} \tag{10}$$

with $\epsilon = \mathrm{sgn}\, C_0$ and $\kappa = h^{\mathcal{I}}/(R_i h)$ ($h^{\mathcal{I}}$ being the strength coefficient related to the interface $\mathcal{I}$), as well as in the macroscopic yield function

$$\widetilde{\mathcal{G}}\left(\widetilde{\mathbf{\Sigma}}^c\right): \quad \begin{cases} \dfrac{\widetilde{\Sigma}_m^c}{h} = \xi\epsilon(1-f)\dfrac{\Psi_m + 3f\kappa\Psi_m^{\mathcal{I}}}{f^{1-\alpha} - f + \epsilon\Psi_m} \\[3mm] \dfrac{\widetilde{\Sigma}_{eq}^c}{h} = \xi\left[3f\kappa\Psi_{eq}^{\mathcal{I}} + \dfrac{f^{1-\alpha} - f - 3f\kappa\epsilon\Psi_m^{\mathcal{I}}}{f^{1-\alpha} - f + \epsilon\Psi_m}\Psi_{eq}\right] \end{cases} \tag{11}$$

where solid matrix (Ψ_m and Ψ_{eq}), and interface ($\Psi_m^{\mathcal{I}}$ and $\Psi_{eq}^{\mathcal{I}}$) model functions can be analytically determined as a function of the macroscopic stress Lode angle $\widetilde{\theta}_\Sigma$. It is worth observing that, by properly calibrating local-yield-function parameters, the macroscopic strength criterion in Eq. (11) straight recovers relationships provided in [1], for a Mohr-Coulomb and a Tresca local plastic responses. Furthermore, in agreement with results provided in [10], the normality law governing the local plastic behavior upscales at the macroscopic level, thereby resulting in a macroscopic normality law with the Lagrange-KKT multiplier in Eq. (10) as plastic multiplier.

Macroscopic yield function in Eq. (11) is represented in Fig. (8), highlighting the effects of principal model parameters on estimated strength properties. For illustrative purposes, reference is made to local yield functions with $(\xi, \beta) \in \{(\xi, \beta) \text{ s.t. } (\xi \geq \xi^*,\ 1 \leq \beta \leq 2)\}$, where $\xi^* = 2/(c_\beta + \sqrt{3}s_\beta)$. As a consequence of the combined dependence on the first I_1^σ and on the third J_3^σ stress invariants of the local yield function, predicted macroscopic strength properties in Fig. (8) are hugely influenced by the macroscopic stress Lode angle $\widetilde{\theta}_\Sigma$, triaxial-compression stress states (that is, TXC$_{\widetilde{\Sigma}}$ for $\widetilde{\theta}_\Sigma = \pi/3$) resulting higher than triaxial-expansion ones (that is, TXE$_{\widetilde{\Sigma}}$ for $\widetilde{\theta}_\Sigma = 0$). Moreover, strength profiles are shown to be pressure-sensitive and strongly asymmetric with respect to the deviatoric axis $\widetilde{\Sigma}_m = 0$, generally predicting higher values for hydrostatic compressive strength than for hydrostatic tensile one. With reference to the case of classical porous materials (that is, for $\kappa \to 0^+$), results in Fig. (8)a show that predicted strength properties increase when the porosity f is reduced, also resulting in a more emphasized asymmetry with respect to the deviatoric axis $\widetilde{\Sigma}_m = 0$. Moreover, for a fixed value of porosity, an overall expansion of the strength profiles TXE$_{\widetilde{\Sigma}}$ and TXC$_{\widetilde{\Sigma}}$ is observed as the local-yield-function parameter β increases. Such an occurrence has to be exclusively ascribed to the description of different local plastic behaviors, not related to any strengthening effect due to the nanosize of voids. On the other hand, when the case of nanoporous materials is addressed (that is, for $\kappa > 0$), results in Fig. (8)b show a significant improvement of macroscopic TXE$_{\widetilde{\Sigma}}$ and TXC$_{\widetilde{\Sigma}}$ strength properties compared to classical porous media, as the parameter κ is increased (namely, when the void size R_i reduces) and the porosity f is considered as fixed. Void-size effects also result in an overall expansion of both TXE$_{\widetilde{\Sigma}}$ and TXC$_{\widetilde{\Sigma}}$ strength profiles along the hydrostatic axis $\widetilde{\Sigma}_{eq} = 0$, mainly affecting macroscopic strength states with a negative hydrostatic component.

5   Conclusions

In this paper, strength properties of nanoporous materials have been investigated via Molecular Dynamics computations and theoretical analyses, providing useful numerical benchmarking evidence and engineering-oriented analytical results. Specifically, numerical calculations have been carried out on in-silico nanoporous aluminium samples undergoing triaxial strain-rate boundary conditions with different deformation paths and a wide range of triaxiality regimes. Effective strength properties of both bulk and nanoporous specimens have been computed, resulting in meridian and deviatoric strength profiles
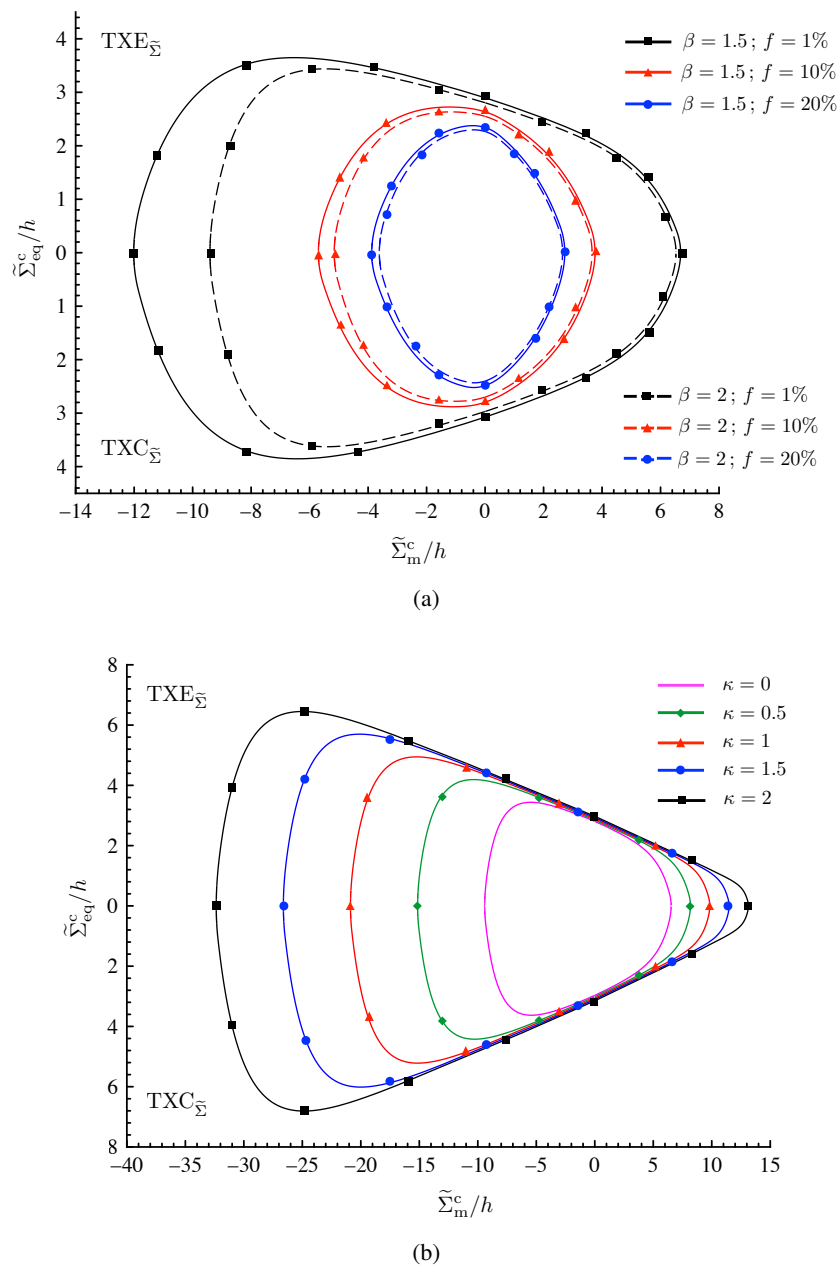
(a)

(b)

Figure 8: Triaxial-expansion (TXE$_{\widetilde{\Sigma}}$) and triaxial-compression (TXC$_{\widetilde{\Sigma}}$) strength profiles for local plastic behaviors such that $(\xi, \beta) \in \{(\xi, \beta) \text{ s.t. } (\xi \geq \xi^*, 1 \leq \beta \leq 2)\}$. (a) Hollow sphere without interface effects (that is, for $\kappa \to 0^+$). (b) Hollow sphere with interface effects (with $f = 1\%$ and $\beta = 2$).

hugely dependent on the Haigh-Westergaard stress invariants. The size-related strengthening effect observed in experimental tests for a fixed porosity level (e.g.,[8]) has been recovered. Physical indications arising from Molecular Dynamics computations clearly suggested the need to consider a rich description of the matrix plastic behavior. To this end, in the framework of a kinematic limit-analysis approach, a macroscopic strength criterion accounting for void-size effects has been derived, by referring to a general-isotropic-plastic hollow sphere with an imperfect-coherent interface at the cavity boundary, and in the case of axisymmetric strain-rate boundary conditions. A parametric expression for the macroscopic strength criterion has been analytically determined as the solution of an inequality-constrained minimization problem, the latter being faced via Karush-Kuhn-Tucker conditions. The resulting macroscopic strength surface is illustrated, as a function of model parameters.

References

[1] K. Anoukou, F. Pastor, P. Dufrenoy, D. Kondo, Limit analysis and homogenization of porous materials with Mohr-Coulomb matrix. Part I: Theoretical formulation, Journal of the Mechanics and Physics of Solids, 91 (2016), 145-171.

[2] D. Bigoni, A. Piccolroaz, Yield criteria for quasibrittle and frictional materials. International Journal of Solids and Structures, 41 (2004), 2855–2878.

[3] S. Brach, L. Dormieux, D. Kondo, D., G. Vairo, A computational insight into void-size effects on strength properties of nanoporous materials, Mechanics of Materials, 101 (2016), 102–117.

[4] S. Brach, L. Dormieux, D. Kondo, D., G. Vairo, Nanoporous materials with a general isotropic plastic matrix: exact limit state under isotropic loadings, International Journal of Plasticity, 89 (2017), 1–28.

[5] L. Dormieux, D. Kondo, An extension of Gurson model incorporating interface stress effects, International Journal of Engineering Science, 48 (2010), 575–581.

[6] L. Dormieux, D. Kondo, Non linear homogenization approach of strength of nanoporous materials with interface effects, International Journal of Engineering Science, 71 (2013), 102–110.

[7] A.L. Gurson, Continuum theory of ductile rupture by void nucleation and growth: Part I. - Yield criterion and flow rules for porous ductile media, Journal of Engineering Materials and Technology, 99 (1977), 2–15.

[8] M. Hakamada, M. Mabuchi, Mechanical strength of nanoporous gold fabricated by dealloying, Scripta Materialia, 56 (2007), 1003–1006.

[9] C. Mi, D.A. Buttry, P. Sharma, D.A. Kouris, Atomistic insights into dislocation-based mechanisms of void growth and coalescence, Journal of the Mechanics and Physics of Solids, 59 (2011), 1858–1871.

[10] J.R. Rice, Inelastic constitutive relations for solids: an internal-variable theory and its application to metal plasticity, Journal of the Mechanics and Physics of Solids, 19 (1971), 433–455.

[11] S. Traiviratana, E.M. Bringa, D.J. Benson, M.A. Meyers, Void growth in metals: Atomistic calculations, Acta Materialia, 56 (2008), 3874–3886.

[12] K.J. Zhao, C.Q. Chen, Y.P. Shen, T.J. Lu, Molecular dynamics study on the nano-void growth in face-centered cubic single crystal copper, Computational Materials Science, 46 (2009), 749–754.